

Temporal and Spatial Scales in Coronal Rain Revealed by UV Imaging and Spectroscopic Observations

Ryohtaroh T. Ishikawa^{1,2} ·
Yukio Katsukawa^{2,1} · Patrick Antolin³ ·
Shin Toriumi⁴

© Springer ●●●

Abstract Coronal rain corresponds to cool and dense clumps in the corona accreting towards the solar surface, and is often observed above solar active regions. They are generally thought to be produced by thermal instability in the corona and their lifetime is limited by the time they take to reach the chromosphere. Although the rain usually fragments into smaller clumps while falling down, their specific spatial and temporal scales remain unclear. In addition, the observational signatures of the impact of the rain with the chromosphere have not been clarified yet. In this study, we investigate the time evolution of velocity and intensity of coronal rain above a sunspot by analyzing coronal images obtained by the Atmospheric Imaging Assembly (AIA) onboard the Solar Dynamics Observatory (SDO) as well as the Slit-Jaw Images (SJIs) and spectral data taken by the Interface Region Imaging Spectrograph (IRIS) satellite. We identify dark and bright threads moving towards the umbra in AIA images and in SJIs, respectively, and co-spatial chromospheric intensity enhancements and redshifts in three IRIS spectra, Mg II k 2796 Å, Si IV 1394 Å, and C II 1336 Å. The intensity enhancements and coronal rain redshifts occur almost concurrently in all the three lines, which clearly demonstrates the causal relationship with

✉ R. T. Ishikawa
ryohtaroh.ishikawa@nao.ac.jp

¹ Department of Astronomical Science, School of Physical Sciences, The Graduate University for Advanced Studies, SOKENDAI, 2-21-1 Osawa, Mitaka, Tokyo 181-8588, Japan

² National Astronomical Observatory of Japan, 2-21-1 Osawa, Mitaka, Tokyo 181-8588, Japan

³ Department of Mathematics, Physics and Electrical Engineering, Northumbria University, Newcastle upon Tyne, NE1 8ST, UK

⁴ Institute of Space and Astronautical Science, Japan Aerospace Exploration Agency, 3-1-1 Yoshinodai, Chuo-ku, Sagami-hara, Kanagawa 2525210, Japan

coronal rain. Furthermore, we detect bursty intensity variation with a timescale shorter than 1 minute in Mg II k, Si IV and C II spectra, indicating that a length scale of rain clumps is about 2.7 Mm if we multiply the typical time scale of the bursty intensity variation at 30 sec by the rain velocity at 90 km s^{-1} . Such rapid enhancements in the IRIS lines are excited within a time lag of 5.6 sec limited by the temporal resolution. These temporal and spatial scales may reflect the physical processes responsible for the rain morphology, and are suggestive of instabilities such as Kelvin-Helmholtz.

Keywords: Coronal rain - Chromosphere - Transition Region - Thermal instability

1. Introduction

The solar corona is known to have average temperatures above a million degrees. However, not all plasmas in the corona have such high temperature: plasma at chromospheric temperatures at coronal heights is commonly observed, particularly above active regions. Coronal rain is one of such cool and dense materials in the corona, usually appearing in chromospheric lines, and subsequently falling along a loop-like path into the chromosphere. Coronal rain was first observed more than 40 years ago (Kawaguchi, 1970; Leroy, 1972). Coronal rain also represents the existence of various dynamic, mass and energy transport processes in coronal loops (Marsch *et al.*, 2008; McIntosh *et al.*, 2012).

Coronal rain is thought to be produced by thermal instability during the catastrophic cooling part of a thermal non-equilibrium (TNE) cycle in which radiative cooling locally overcomes the coronal heating mechanisms as demonstrated in a one-dimensional numerical simulations (Parker, 1953; Müller, Hansteen, and Peter, 2003; Müller, Peter, and Hansteen, 2004; Müller *et al.*, 2005; Xia *et al.*, 2011). The TNE cycle is induced by concentrated heating localized nearer to the chromospheric footpoints than to the loop apex (Antiochos and Klimchuk, 1991). Chromospheric evaporation and density increase in the loop is induced by the heating, which increases radiative losses in the corona and results in a loss of thermal equilibrium and catastrophic cooling for sustained footpoint heating. Recently, Fang, Xia, and Keppens (2013) and Fang *et al.* (2015) studied the formation and the evolution of the coronal rain using 2.5-dimensional models and showed that multiple clumps in a coronal loop induce siphon flows which cause shear flows and deform the falling clumps themselves.

The cooling sequence of the loops has been also investigated using several observations by the Transition Region and Coronal Explorer (Schrijver, 2001) and Extreme Ultraviolet Imaging Telescope onboard Solar and Heliospheric Observatory (e.g. de Groof *et al.* 2005), which detected EUV intensity variations of coronal loops in ARs. Antolin *et al.* (2015) showed that chromospheric emission follows the observed cooling in the EUV lines, as expected from catastrophic cooling events. EUV intensity pulsation with long-term periods were observed in warm coronal loops (Auchère *et al.*, 2014; Froment *et al.*, 2015, 2017) and shown to match well with TNE cycles. Antolin, Shibata, and Vissers (2010)

argued that coronal rain may point to the agent of the heating of coronal loops as well as the spatial distribution of the heating in loops using a combination of Hinode observations and loop modelling of Alfvénic wave heating.

Antolin *et al.* (2015) coordinated observations with high-resolution and multi-wavelength instruments, and obtained the specific spatial scale of the coronal rains at each temperature. The most frequent scales of width and length detected in 1400 Å slit-jaw images (SJIs) taken by Interface Region Imaging Spectrograph (IRIS: De Pontieu *et al.* 2014) are 0".88 and 1".76, respectively. Antolin, Vissers, and Rouppe van der Voort (2012) and Antolin and Rouppe van der Voort (2012) analyzed off-limb and on-disk H α observation data obtained with the CRisp Imaging SpectroPolarimeter at the Swedish Solar Telescope and detected cool and dense clump-like structures. They interpreted the clumps as coronal rain based on their spectral and morphological characteristics. In particular they showed that the rain morphology is clumpy and multi-stranded at high resolution, with an average length distribution of 700 km with a long tail towards longer lengths, and an average width distribution of 300 km with a full-width at half maximum (FWHM) of 100 km. At the same time, they also concluded that there exists undetected, even smaller clumps because the current spatial resolution is not enough.

Kleint *et al.* (2014) reported the first observation tracing coronal rain into an umbra and associated bright dots with IRIS. They interpreted that the coronal rain falls down along loops and collides with the local plasma in the transition region (TR), increasing density and temperature in the TR above a sunspot. In the IRIS spectral lines, rain is observed as bursts of strong Doppler shifts with an average duration of 20s, indicating supersonic downward flows of up to 200 km s⁻¹ just prior to impact, which is faster than the free fall velocity for a plasma initially at rest.

In this article, we estimate the temporal and spatial scales from observational data obtained by IRIS and SDO. The rest of the article proceeds as follows. In Section 2, we introduce the data that we use. In Section 3, we describe the analysis and results. In Section 4, we summarize and discuss the observational results from the view point of scales in the coronal rain.

2. Observations

For this study, we analyze the observational data of active region (AR) NOAA 12042 obtained by IRIS and the Solar Dynamics Observatory (SDO: Pesnell, Thompson, and Chamberlin 2012). IRIS observed AR 12042 with the sit-and-stare mode of IRIS and Hinode Operation Plan (IHOP) 250 from 10:00 to 11:15 UT on 24 April 2014, providing spectral data in three lines (C II 1336 Å, Si IV 1396 Å, and Mg II k 2796 Å). The slit width is 0".33 and the pixel size and slit length are 0".166 and 119", respectively. IRIS also produced simultaneous SJIs data in 1400 Å and 2796 Å, whose field of view is about 119" \times 119". The recording cadences of spectral data and SJIs are 5.6 s and 11 s, respectively. The central sunspot in AR 12042 was located at (x, y)=(475", 359") at the beginning of the IRIS observation. We used the level 2 data, where dark-current

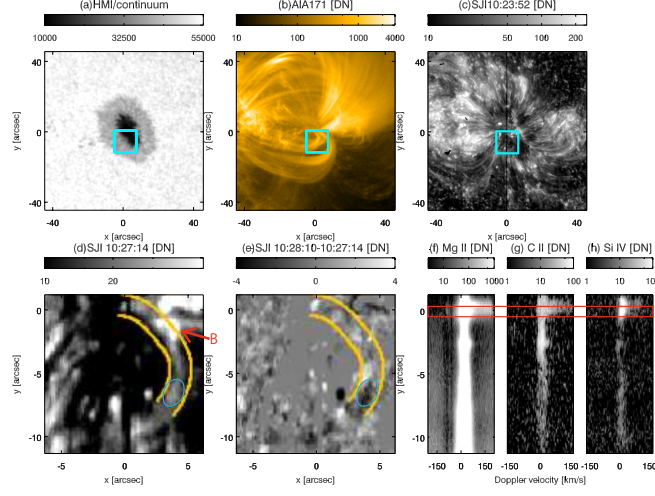


Figure 1. AR NOAA 12042 and coronal rain observed on 24 April 2014. (a), (b) and (c) show the target AR obtained by SDO/Heliioseismic and Magnetic Imager continuum, SDO/AIA 171 Å and IRIS/SJI at Si IV line (1400 Å), respectively. A close-up image of IRIS/SJI at Si IV line (panel d) and a difference between two IRIS/SJI images with a time difference of 56 seconds (panel e) showing that a bright thread-like structure (indicated by a blue circle) moves along a loop-like path (indicated by the yellow curves) to the sunspot umbra. These yellow curves are determined by the loop-like structure seen in the AIA 171Å image (Panel b). The blue rectangles in (a), (b), and (c) correspond to the field-of-view (FOV) of (d) and (e). The IRIS spectra of Mg II k line 2796 Å (f), Si IV line 1396 Å, and (g) and C II line 1336 Å (h) at 10:37:54 UT. The red rectangle indicates the region where we take the average of the spectra to obtain the temporal evolution of the intensity of each IRIS spectral line. The movie corresponding to panels d and f–h can be found in the additional material; this is the file movie1.mpeg. In this movie we also show the close-up image in AIA 171 Å.

subtraction, flat-field correction, and geometric and wavelength calibration are applied.

The target AR was also covered by the Atmospheric Imaging Assembly (AIA: Lemen *et al.* 2012) onboard the SDO satellite, which makes synoptic observations in multiple wavelengths in the EUV with a cadence of 12 s. In this study, we mainly used the 171 Å channel images to investigate the morphology and evolution.

3. Results

3.1. Overview of the Observed Region

Panels a, b and c in Figure 1 show the image of the active region obtained by SDO/HMI continuum, SDO/AIA at 171 \AA ($\log T = 5.8$), and IRIS/SJI at Si IV line (1400 \AA , $\log T = 4.9$) respectively. Panel d shows a close-up image of IRIS/SJI at Si IV line and panel e shows a difference between two images of IRIS/SJI, showing that a bright clump moves along a loop-like trajectory leading into an umbra. Panels f–h show spectrograph of Mg II k (2796 \AA , $\log T = 4$), C II (1336 \AA , $\log T = 4.4$) and Si IV (1396 \AA , $\log T = 4.9$) obtained by IRIS sit-and-stare mode. The sunspot umbra is located at the center of the FOV shown in panels b–e, and is overlapped by the IRIS slit. The horizontal axis of the spectral data f–h is the Doppler velocity, where positive and negative indicate the red and blueshifts, respectively.

One can see a bright, thread-like structure falling down to the sunspot umbra along a loop-like path as indicated by the yellow lines in Figures 1d and e. The loop-like path coincides with a loop seen in the image in AIA 171 \AA . This path ends just at the IRIS slit which overlaps the umbra. In addition, there are some clumps moving along this path (see the movie that accompanies this article, movie1.mpeg). At the same time, in the IRIS spectral data (panels f–h), all the three lines show redshifts coinciding with the fall of the clumps at the footpoint of the trajectory. This indicates that the clumps have a multi-temperature structure ($4 < \log T < 4.9$, Antolin et al. 2015). The observed features of this bright thread match the characteristics of the coronal rain (Antolin, Vissers, and Rouppe van der Voort, 2012; Kleint *et al.*, 2014).

3.2. Temporal Evolution of Coronal Rain

Figures 2a–c show the time evolutions of IRIS spectra at the footpoint from 10:00:28 UT on 24 April 2014. We use spectra averaged over 5 pixels along the slit, corresponding to a width of 580 km. The horizontal axis indicates the Doppler velocity.

Figures 2d and e show distance-time diagrams along the trajectory of the rain seen in IRIS 1400 \AA SJI (Figure 1a) and AIA 171 \AA , respectively. We use the distance along the trajectory of the coronal rain indicated by the yellow curves in Figures 1d and e, and define the origin of the rain footpoint on the IRIS slit. We averaged the data over 11 pixels perpendicular to the trajectory. In Figure 2d, we can see some bright clumps, indicating the coronal rain, moving toward the umbra along the path in SJI 1400 \AA . Although there is another bright structure near the slit (at about 2 Mm from the origin; as indicated by B in Figure 1d), the motion of coronal rain is not affected by the structure, probably because the structure and coronal rain overlap along the line-of-sight due to the projection effect.

Because there are stationary and highly red-shifted components in the spectra observed with IRIS, we estimated the Doppler velocity of the coronal rain using the IRIS spectral data with the following method. First, we defined the central

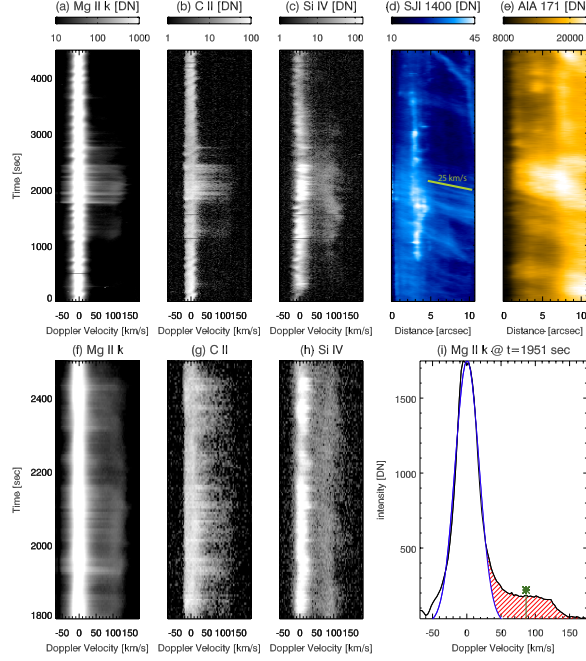


Figure 2. Time evolution for: (a) Mg II k, (b) C II, and (c) Si IV lines as a function of Doppler shift. The origin of time axis is defined as 10:00:28 UT on 24 April 2014. (d) and (e) show the time evolutions for the IRIS/SJI 1400 Å images and SDO/AIA 171 Å along the loop-like trajectory indicated as yellow curves in Figure 1d. The IRIS slit is located at the origin. Bright threads (coronal rain) move toward the slit and reach there, especially in the range $1800 \text{ s} \leq t \leq 2500 \text{ s}$. At the same time, all the lines show large redshifts. (f), (g), and (h) show close-up time intervals of (a), (b), and (c), respectively. (i) shows the spectrum of Mg II k line at $t = 1951 \text{ s}$ (black line), the stationary component detected by a single Gaussian fitting (blue line), and the redshifted component defined as the residual (red region). The center of gravity is described as a green line in (i), which indicates the redshifted velocity at that moment.

wavelength of the stationary component by applying a Gaussian fit to the IRIS spectra and its intensity by integrating the obtained Gaussian profile (the blue line in Figure 2i). After subtracting the stationary component from the original spectra, we then measured the integrated intensity and the center of gravity of the residual spectra as the intensity and the Doppler velocity of the secondary component representing the coronal rain (the red region in Figure 2i).

In the IRIS spectra (Figures 2a–c), the intensity enhancements and redshift are observed at the same time when the coronal rain reaches the position of the slit from 1800 to 2500 s, as shown in Figure 2d. The mean Doppler velocity of the coronal rain is about 85 km s^{-1} in the Si IV line, while the plane-of-sky velocity along the trajectory (yellow curve in Figures 1d and e) is about 25 km s^{-1} , which is measured by the slope in the distance-time diagram when the rain reaches the slit ($1800 \text{ s} < t < 2500 \text{ s}$) in Figure 2d. This indicates that the rain drops at an absolute velocity of 90 km s^{-1} and that the rain trajectory prior to

impact is mostly directed along the line-of-sight. In addition, we can see weaker upflows besides the strong downflows. We discuss the upflows in Section 4.

3.3. Temporal Variation of the IRIS Spectral Data

There are two types of variability seen in the temporal variation of the IRIS spectra shown in Figures 2a–c. One is the saw-tooth continuous variation, and the other are short-term bursts (Figures 2f–h). The saw-tooth variation is seen over the whole observation period, whereas the bursty one is seen only when the rain reaches the IRIS slit ($1800 \text{ s} \leq t \leq 2500 \text{ s}$). This indicates that the bursty variation has an association with the coronal rain. In order to estimate the timescale of these saw-tooth and bursty variations, we did a wavelet analysis.

The time series of intensity variations of the stationary component is derived by the total intensity of a single gaussian fitting as shown by the blue line in Figure 2i. The intensity variation of the redshifted components is defined by the total intensity of the residual described as the red region in Figure 2i. The intensity variations of both the stationary and the redshifted components are normalized with the noise levels measured at the end of the data ($t > 3900 \text{ s}$) as explained in Gabriel *et al.* (2002). Figure 3a shows the wavelet power spectra for the intensity variation of the stationary component of Mg II k line. We computed the time-averaged wavelet spectra in the way developed in Auchère *et al.* (2016) and fitted them with power law functions (Kayshap *et al.*, 2020):

$$\sigma(\nu) = A\nu^s, \quad (1)$$

where A , ν , and s are a coefficient, frequency, and a power law index, respectively. The 90% global confidence levels are calculated based on $\sigma(\nu)$ (Auchère *et al.*, 2016). In Figure 4 we show the time-averaged wavelet spectra (blue solid lines), the power law fits (blue dashed lines), the wavelet power spectra at $t=1920 \text{ s}$ (black solid lines), and the 90% confidence levels (red solid lines) for Mg II k (left) and Si IV (right). The figure demonstrates how the power law function $\sigma(\nu)$ is obtained by fitting of the wavelet power spectra. Figures 3b–d show the wavelet spectra for the stationary components of Mg II k, C II, and Si IV lines normalized with $\sigma(\nu)$, and panels (e) and (f) are the same figures as panels (b) and (c) but for the intensity variation of the redshifted components. There is a component with 3 minute periodicity all over the time series, which is clearly seen especially in the Mg II k line (Figures 3a and b). This corresponds to the 3 minute sunspot oscillation, which behaves as a shock wave as it propagates from the chromosphere to the TR, including impulsive blueshifts accompanied by intensity enhancements (Tian *et al.*, 2014). On the other hand, the short-term component with a period shorter than 1 minute corresponding to the bursty variation has large power only in the period when the rain reaches the IRIS slit (from 1800 to 2500 s), which may indicate that the short-term variation is excited by the coronal rain, although the wavelet power spectra of the short-term component are broad.

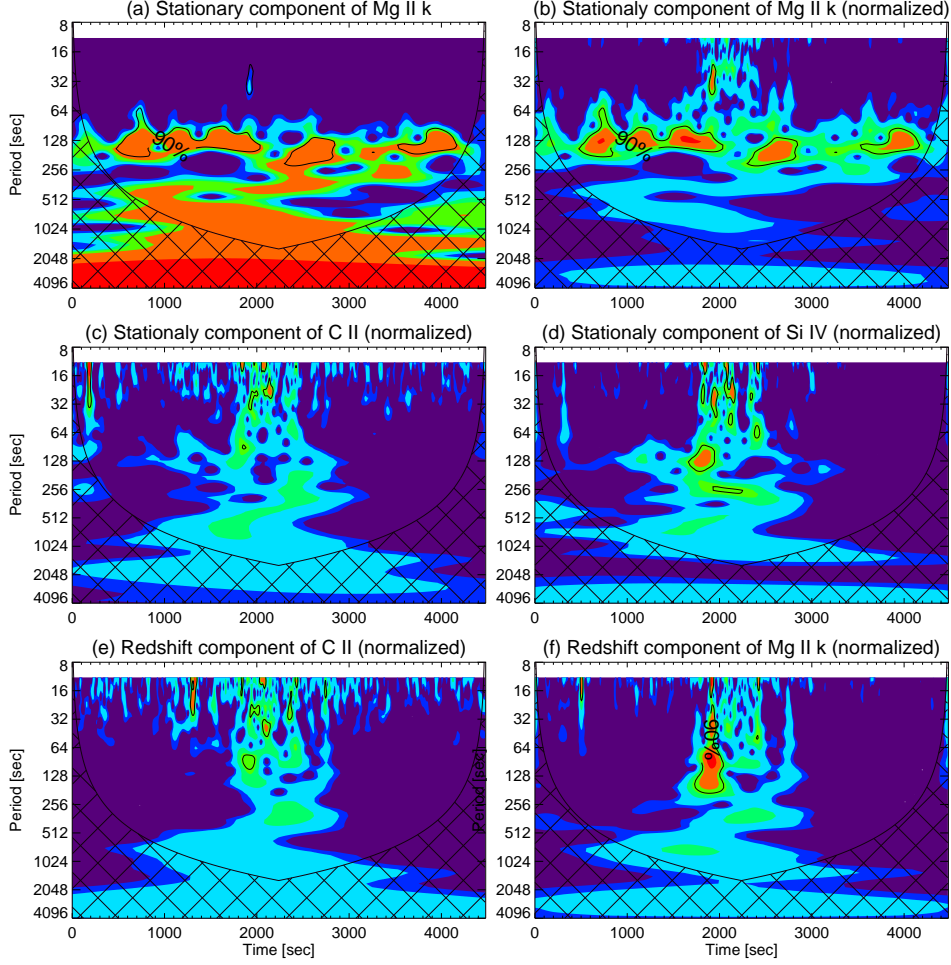


Figure 3. (a) The wavelet power spectrum for the intensity variation of the stationary component of Mg II k. (b)-(d) The wavelet power spectra for the intensity variation of the stationary component of Mg II k, C II, and Si IV normalized with $\sigma(\nu)$ defined in Equation 1. (e)-(f) The wavelet power spectra for the intensity variation of the redshifted components of Mg II k and C II normalized with $\sigma(\nu)$. The black contours indicate the confidence level of 90% computed with $\sigma(\nu)$. The time-axis is the same as that of Figure 2.

3.4. Time Lag of the Intensity Enhancements among the Lines

For revealing the nature of intensity enhancements, it is important to clarify the temporal order of the intensity enhancements between the three IRIS lines. We calculated the cross-correlation coefficients between the intensity variations of Mg II k and those of Si IV and C II as functions of time lag at each time-scale, as shown in Figure 5. Since the IRIS spectral data were taken simultaneously by the three lines according to time stamps in the data, we do not need interpolation of the time series for calculating cross-correlation coefficients between them. As

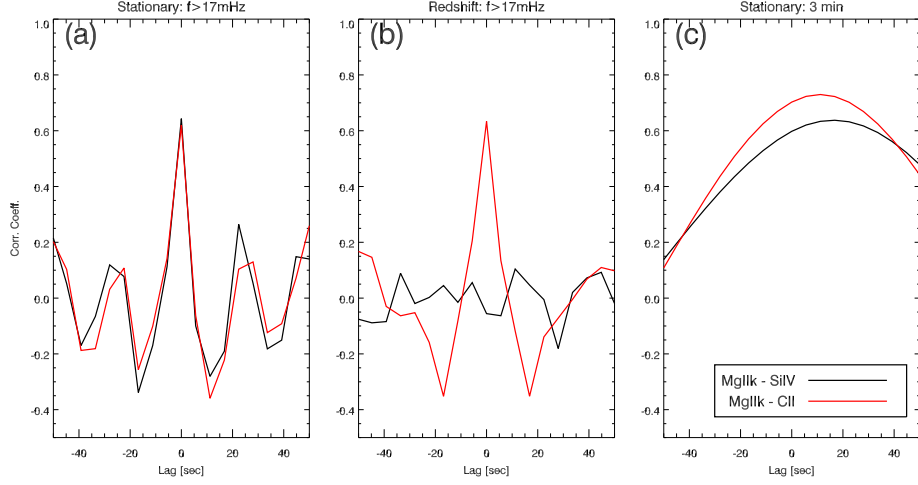


Figure 4. Wavelet power spectra of the stationary components of Mg II k (left) and Si IV (right). The blue solid lines show the time-averaged wavelet spectra and the blue dashed lines show the power law fits $\sigma(\nu)$ of them. The black solid lines show the wavelet power spectra at $t=1920$ s and the red solid lines show the 90% confidence levels calculated with $\sigma(\nu)$.

we see in Figure 3, there are two types of intensity variations: the saw-tooth continuous variation with a periodicity of 3 minutes and the short-term bursts with a timescale shorter than 1 minutes. Therefore we calculated the cross-correlation coefficient for each type of intensity variation extracted from the original intensity variation with band-pass and high-pass filters.

Figure 5a shows the correlation functions of stationary components derived with a high-pass filter that extracts the short-term variation from the original time-series. We use a high-pass filter with the cut-off frequency around 17 mHz (corresponding to 1 minutes) and with a cosine roll-off. The short-term variations of the stationary component have correlation coefficients larger than 0.6 at a time lag of 0 seconds although determination of the peak time lag is limited by the time cadence of the IRIS spectral data (5.6 sec).

Figure 5b is the same as the one in panel a but for the redshifted component. The correlation coefficient between the intensity variations of Mg II k and C II has large correlation coefficients like those seen in panel a, whereas that between Mg II k and Si IV has almost no correlation, which is probably due to the low signal-to-noise ratio of the redshifted component of Si IV.

Figure 5c is the same as that in panel a but processed with a band-pass filter that extracts 3 minutes variation. The full width of this band-pass filter is 5.1 mHz in the frequency domain. In contrast to the correlation coefficients of the short-term variation shown in Figures 5a and b, the intensities of the IRIS lines are enhanced in the order of Mg II k, C II, and Si IV in 3 minutes variation, indicating that such enhancements occur in increasing temperature order, from the lower atmosphere. The intensity enhancements in C II and Si IV lag the Mg II k by 11.2 and 16.8 seconds, respectively. Similar repeated patterns have been reported for dynamic fibrils in plagues and for sunspots (Tian *et al.*, 2014) and

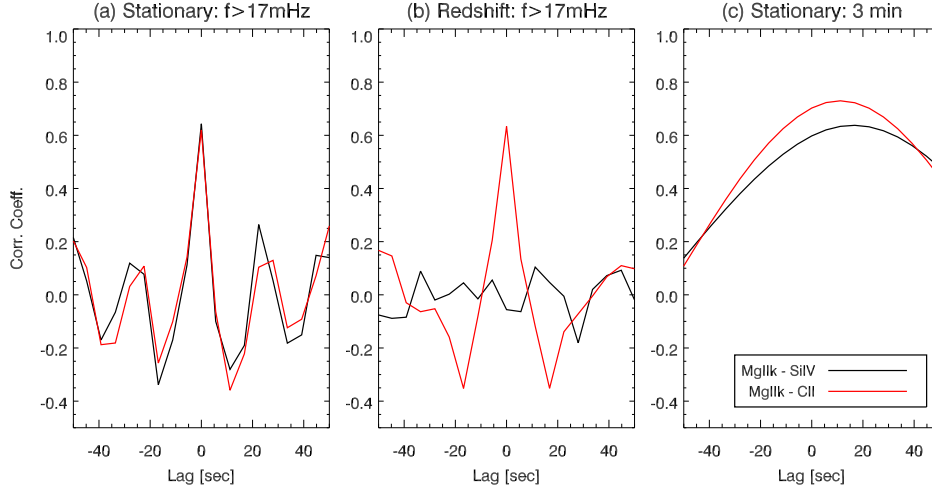


Figure 5. Cross-correlation coefficients between intensity variations of Mg II k and those of Si IV and C II as a function of time lag in the rain time (from 1800 s to 2500 s), where positive time lag means the Mg II k line precedes; correlation functions (a) for short timescale intensity variations of the stationary components, (b) for short-term intensity variations with a timescale shorter than 1 min of the redshift components, (c) for 3 minute intensity variations of the stationary components. We use a high-pass filter with the cut-off frequency is around 17 mHz and with a cosine roll-off for (a) and (b) and use a rectangle band-pass filter with a full width of 5.1 mHz for (c) to extract specific timescale components from the original data.

they concluded that such patterns are driven by dynamic chromospheric shock waves. The saw-tooth periodic structure seen in Figure 2a consisting of impulsive blueshifts accompanied by gradual redshifts also supports this interpretation.

4. Summary and Discussion

In the previous section, we estimated the properties of the on-disk coronal rain moving towards the sunspot umbra. The coronal rain clumps fall with Doppler velocity and plane-of-sky velocity of 85 km s^{-1} and 25 km s^{-1} , respectively, which yields an actual velocity of 90 km s^{-1} , i.e., much faster than the local sound speeds in the TR and the chromosphere since the local sound speed is $10 - 50 \text{ km s}^{-1}$ when the temperature is $10^4 - 10^5 \text{ K}$ if we use an adiabatic sound speed of $\sqrt{\gamma k_B T / m}$ where γ , k_B , T , and m are the heat capacity ratio, the Boltzmann constant, temperature, and mass of a particle, respectively. As shown in Figures 5a and b, there are no significant time-lags between the short-term intensity variations of the three IRIS lines. These results indicate that all the lines are heated up concurrently, most probably due to shock waves induced by the supersonic coronal rain. This local heating interpretation is also consistent with the weaker upflows besides the strong downflows seen in Figure 2. These weaker upflows suggest that mild evaporation is produced by the heating by the coronal rain besides the strong downflows seen at the Mg II k line in Figure 2f (Kleint *et al.*, 2014). The coronal rain clumps have a width of 580 km and show

rapid intensity fluctuations with a timescale shorter than 1 minute. Hereafter we use typical timescale of the coronal rain of 30 seconds. If we multiply the timescale of 30 sec by the velocity of 90 km s^{-1} , the typical length of the clumps is estimated to be about 2.7 Mm. Such widths and lengths are consistent with those observed in the same lines and instrument by Antolin *et al.* (2015). The temperature should be about 10^5 K equivalent to the formation temperature of the Si IV line.

The clear relationship between the apparent flows falling onto the sunspot umbra and the intensity enhancements of stationary components with strong Doppler shift suggest that the coronal rain induces the local heating events. These heating events are possibly due to the shock made by the supersonic downflows of the coronal rain. The general scenario of the local heating by the coronal rain is the same as in previous reports (Kleint *et al.*, 2014; Reale *et al.*, 2013). However, the location of the shock front, or equivalently the height of the plasma heating, remains unclear. The falling material can penetrate the atmosphere to a dense layer whose gas pressure is equal to the ram pressure of the rain. The ram pressure $P_{ram} = \frac{1}{2}\rho v^2$ is estimated about 9.5 dyn cm^{-2} , where we use observed velocity 90 km s^{-1} and previously reported average electron density $1.4 \times 10^{11} \text{ cm}^{-3}$ (Antolin *et al.*, 2015).

When the coronal rain collides with the chromospheric plasma, a part of the kinetic energy of coronal rain is converted into thermal energy, heating chromospheric plasma and the falling coronal rain. We can estimate the amount of the kinetic energy of a clump of the coronal rain E_{clump} to be

$$E_{clump} = \frac{1}{2}\rho v^2 V_{clump} = \frac{1}{2}m_p n_e v^2 (\pi r^2 l), \quad (2)$$

where V_{clump} is the volume of a clump, and we approximate its shape by a cylinder with the radius r and the length l . In this case, the radius is equivalent to the half of the clump's width of 580 km corresponding to 5 IRIS pixels. We use the electron density $1.4 \times 10^{11} \text{ cm}^{-3}$. If we apply the observed values, $r = 290 \text{ km}$, $l = 2.7 \text{ Mm}$, and $v = 90 \text{ km s}^{-1}$, then we get the kinetic energy of about $6.8 \times 10^{24} \text{ erg}$. Let us assume the condition that the number density in the chromosphere is 10^{12} cm^{-3} and the volume is $\pi r^2 H$, where $H = 300 \text{ km}$ is the pressure scale height of the chromosphere. If the temperature increase from $\log T = 4$ to $\log T = 5$, the required heating energy $n k_B \Delta T (\pi r^2 H)$ is estimated to be about $1 \times 10^{24} \text{ erg}$. Therefore, by converting a fraction of the kinetic energy, the coronal rain can heat the chromosphere.

The most important question is what produces such small-scale structures. When a coronal rain clump is first produced in the corona, the typical size of the clump may reflect the spatial scales of dynamical processes within the loops. In principle, a condensation will form and accumulate plasma as long as a pressure gradient exists. This pressure gradient is created initially by the loss of pressure from thermal instability. During its precipitation from the corona to the lower layers, the coronal rain clump could be broken into a smaller pieces by the Kelvin-Helmholtz instability (KHI) excited by the velocity shear between the clump and the surrounding stationary atmosphere. However, if the velocity vector of the coronal rain clump is parallel to the magnetic field, the KHI may not grow

easily since the magnetic tension is likely to suppress KHI vortices. In 2.5-D MHD simulations by Fang *et al.* (2015) both very long and short clumps can be formed. Although their simulation does not provide the sufficient resolution to investigate the formation of the KHI, they discuss how the shear flows could lead to the break-up of the clumps, and they suggest a possible influence of the KHI. On the other hand, Martínez-Gómez *et al.* (2019) performed two-dimensional ideal MHD simulation of coronal rain and concluded that the KHI are not expected to develop in typical coronal rain conditions. They argued that the length of coronal rain may be explained by the timescale of the catastrophic cooling. Future high-resolution and multi-wavelength observations such as Solar-C/EUV High-Throughput Spectroscopic Telescope (EUVST: Shimizu *et al.* 2019) will reveal the formation mechanism of clumps in coronal rain.

Acknowledgments Data are a courtesy of the science teams, IRIS and SDO. IRIS is a NASA small explorer mission developed and operated by LMSAL with mission operations executed at NASA Ames Research center and major contributions to downlink communications funded by ESA and the Norwegian Space Centre. AIA is an instrument on board SDO, a mission for NASA’s Living with a Star program. R.T.I. is supported by JSPS Research Fellowships for Young Scientists. P.A. acknowledges funding from his STFC Ernest Rutherford Fellowship (No. ST/R004285/1). This work was supported by JSPS KAKENHI Grant Numbers JP16K17671 (PI: S. Toriumi), JP15H05814 (PI: K. Ichimoto), JP25220703 (PI: S. Tsuneta), JP18H05234 (PI: Y. Katsukawa), and JP19J20294 (PI: R.T. Ishikawa).

Disclosure of Potential Conflicts of Interest The authors declare that there are no conflicts of interest.

References

- Antiochos, S.K., Klimchuk, J.A.: 1991, A model for the formation of solar prominences. *Astrophys. J.* **378**, 372. DOI. ADS.
- Antolin, P., Rouppe van der Voort, L.: 2012, Observing the Fine Structure of Loops through High-resolution Spectroscopic Observations of Coronal Rain with the CRISP Instrument at the Swedish Solar Telescope. *Astrophys. J.* **745**, 152. DOI. ADS.
- Antolin, P., Shibata, K., Vissers, G.: 2010, Coronal Rain as a Marker for Coronal Heating Mechanisms. *Astrophys. J.* **716**, 154. DOI. ADS.
- Antolin, P., Vissers, G., Rouppe van der Voort, L.: 2012, On-Disk Coronal Rain. *Solar Phys.* **280**, 457. DOI. ADS.
- Antolin, P., Vissers, G., Pereira, T.M.D., Rouppe van der Voort, L., Scullion, E.: 2015, The Multithermal and Multi-stranded Nature of Coronal Rain. *Astrophys. J.* **806**, 81. DOI. ADS.
- Auchère, F., Bocchialini, K., Solomon, J., Tison, E.: 2014, Long-period intensity pulsations in the solar corona during activity cycle 23. *Astron. Astrophys.* **563**, A8. DOI. ADS.
- Auchère, F., Froment, C., Bocchialini, K., Buchlin, E., Solomon, J.: 2016, On the Fourier and Wavelet Analysis of Coronal Time Series. *Astrophys. J.* **825**(2), 110. DOI. ADS.
- de Groof, A., Bastiaansen, C., Müller, D.A.N., Berghmans, D., Poedts, S.: 2005, Detailed comparison of downflows seen both in EIT 30.4 nm and Big Bear H α movies. *Astron. Astrophys.* **443**, 319. DOI. ADS.
- De Pontieu, B., Title, A.M., Lemen, J.R., Kushner, G.D., Akin, D.J., Allard, B., Berger, T., Boerner, P., Cheung, M., Chou, C., Drake, J.F., Duncan, D.W., Freeland, S., Heyman, G.F., Hoffman, C., Hurlburt, N.E., Lindgren, R.W., Mathur, D., Rehse, R., Sabolish, D., Seguin, R., Schrijver, C.J., Tarbell, T.D., Wülser, J.-P., Wolfson, C.J., Yanari, C., Mudge, J., Nguyen-Phuc, N., Timmons, R., van Bezooijen, R., Weingrod, I., Brookner, R., Butcher,

- G., Dougherty, B., Eder, J., Knagenhjelm, V., Larsen, S., Mansir, D., Phan, L., Boyle, P., Cheimets, P.N., DeLuca, E.E., Golub, L., Gates, R., Hertz, E., McKillop, S., Park, S., Perry, T., Podgorski, W.A., Reeves, K., Saar, S., Testa, P., Tian, H., Weber, M., Dunn, C., Eccles, S., Jaeggli, S.A., Kankelborg, C.C., Mashburn, K., Pust, N., Springer, L., Carvalho, R., Kleint, L., Marmie, J., Mazmanian, E., Pereira, T.M.D., Sawyer, S., Strong, J., Worden, S.P., Carlsson, M., Hansteen, V.H., Leenaarts, J., Wiesmann, M., Aloise, J., Chu, K.-C., Bush, R.I., Scherrer, P.H., Brekke, P., Martínez-Sykora, J., Lites, B.W., McIntosh, S.W., Uitenbroek, H., Okamoto, T.J., Gummin, M.A., Auker, G., Jerram, P., Pool, P., Waltham, N.: 2014, The Interface Region Imaging Spectrograph (IRIS). *Solar Phys.* **289**, 2733. DOI. ADS.
- Fang, X., Xia, C., Keppens, R.: 2013, Multidimensional Modeling of Coronal Rain Dynamics. *Astrophys. J. Lett.* **771**, L29. DOI. ADS.
- Fang, X., Xia, C., Keppens, R., Van Doorselaere, T.: 2015, Coronal Rain in Magnetic Arcades: Rebound Shocks, Limit Cycles, and Shear Flows. *Astrophys. J.* **807**, 142. DOI. ADS.
- Froment, C., Auchère, F., Bocchialini, K., Buchlin, E., Guennou, C., Solomon, J.: 2015, Evidence for Evaporation-incomplete Condensation Cycles in Warm Solar Coronal Loops. *Astrophys. J.* **807**, 158. DOI. ADS.
- Froment, C., Auchère, F., Aulanier, G., Mikić, Z., Bocchialini, K., Buchlin, E., Solomon, J.: 2017, Long-period Intensity Pulsations in Coronal Loops Explained by Thermal Non-equilibrium Cycles. *Astrophys. J.* **835**, 272. DOI. ADS.
- Gabriel, A.H., Baudin, F., Boumier, P., García, R.A., Turck-Chièze, S., Appourchaux, T., Bertello, L., Berthomieu, G., Charra, J., Gough, D.O., Pallé, P.L., Provost, J., Renaud, C., Robillot, J.-M., Roca Cortés, T., Thiery, S., Ulrich, R.K.: 2002, A search for solar g modes in the GOLF data. *Astron. Astrophys.* **390**, 1119. DOI. ADS.
- Kawaguchi, I.: 1970, Observed Interaction between Prominences. *Pub. Astron. Soc. Japan* **22**, 405. ADS.
- Kayshap, P., Srivastava, A.K., Tiwari, S.K., Jelínek, P., Mathioudakis, M.: 2020, Propagation of waves above a plage as observed by IRIS and SDO. *Astron. Astrophys.* **634**, A63. DOI. ADS.
- Kleint, L., Antolin, P., Tian, H., Judge, P., Testa, P., De Pontieu, B., Martínez-Sykora, J., Reeves, K.K., Wuelser, J.P., McKillop, S., Saar, S., Carlsson, M., Boerner, P., Hurlburt, N., Lemen, J., Tarbell, T.D., Title, A., Golub, L., Hansteen, V., Jaeggli, S., Kankelborg, C.: 2014, Detection of Supersonic Downflows and Associated Heating Events in the Transition Region above Sunspots. *Astrophys. J. Lett.* **789**, L42. DOI. ADS.
- Lemen, J.R., Title, A.M., Akin, D.J., Boerner, P.F., Chou, C., Drake, J.F., Duncan, D.W., Edwards, C.G., Friedlaender, F.M., Heyman, G.F., Hurlburt, N.E., Katz, N.L., Kushner, G.D., Levay, M., Lindgren, R.W., Mathur, D.P., McFeaters, E.L., Mitchell, S., Rehse, R.A., Schrijver, C.J., Springer, L.A., Stern, R.A., Tarbell, T.D., Wuelser, J.-P., Wolfson, C.J., Yanari, C., Bookbinder, J.A., Cheimets, P.N., Caldwell, D., DeLuca, E.E., Gates, R., Golub, L., Park, S., Podgorski, W.A., Bush, R.I., Scherrer, P.H., Gummin, M.A., Smith, P., Auker, G., Jerram, P., Pool, P., Soufi, R., Windt, D.L., Beardsley, S., Clapp, M., Lang, J., Waltham, N.: 2012, The Atmospheric Imaging Assembly (AIA) on the Solar Dynamics Observatory (SDO). *Solar Phys.* **275**, 17. DOI. ADS.
- Leroy, J.-L.: 1972, Emissions 'froides' dans la couronne solaire. *Solar Phys.* **25**, 413. DOI. ADS.
- Marsch, E., Tian, H., Sun, J., Curdt, W., Wiegmann, T.: 2008, Plasma Flows Guided by Strong Magnetic Fields in the Solar Corona. *Astrophys. J.* **685**, 1262. DOI. ADS.
- Martínez-Gómez, D., Oliver, R., Khomenko, E., Collados, M.: 2019, Two-dimensional simulations of coronal rain dynamics. I. Model with vertical magnetic field and an unbounded atmosphere. *arXiv e-prints*, arXiv:1911.06638. ADS.
- McIntosh, S.W., Tian, H., Sechler, M., De Pontieu, B.: 2012, On the Doppler Velocity of Emission Line Profiles Formed in the "Coronal Contraflow" that Is the Chromosphere-Corona Mass Cycle. *Astrophys. J.* **749**, 60. DOI. ADS.
- Müller, D.A.N., Hansteen, V.H., Peter, H.: 2003, Dynamics of solar coronal loops. I. Condensation in cool loops and its effect on transition region lines. *Astron. Astrophys.* **411**, 605. DOI. ADS.
- Müller, D.A.N., Peter, H., Hansteen, V.H.: 2004, Dynamics of solar coronal loops. II. Catastrophic cooling and high-speed downflows. *Astron. Astrophys.* **424**, 289. DOI. ADS.
- Müller, D.A.N., De Groof, A., Hansteen, V.H., Peter, H.: 2005, High-speed coronal rain. *Astron. Astrophys.* **436**, 1067. DOI. ADS.
- Parker, E.N.: 1953, Instability of Thermal Fields. *Astrophys. J.* **117**, 431. DOI. ADS.

- Pesnell, W.D., Thompson, B.J., Chamberlin, P.C.: 2012, The Solar Dynamics Observatory (SDO). *Solar Phys.* **275**, 3. DOI. ADS.
- Reale, F., Orlando, S., Testa, P., Peres, G., Landi, E., Schrijver, C.J.: 2013, Bright Hot Impacts by Erupted Fragments Falling Back on the Sun: A Template for Stellar Accretion. *Science* **341**, 251. DOI. ADS.
- Schrijver, C.J.: 2001, Catastrophic cooling and high-speed downflow in quiescent solar coronal loops observed with TRACE. *Solar Phys.* **198**, 325. DOI. ADS.
- Shimizu, T., Imada, S., Kawate, T., Ichimoto, K., Suematsu, Y., Hara, H., Katsukawa, Y., Kubo, M., Toriumi, S., Watanabe, T., Yokoyama, T., Korendyke, C.M., Warren, H.P., Tarbell, T., Pontieu, B.D., Teriaca, L., Schhle, U.H., Solanki, S., Harra, L.K., Matthews, S., Fludra, A., Auchre, F., Andretta, V., Naletto, G., Zhukov, A.: 2019, The Solar-C_EUVST mission. In: Siegmund, O.H. (ed.) *UV, X-Ray, and Gamma-Ray Space Instrumentation for Astronomy XXI* **11118**, SPIE, ???, 27. International Society for Optics and Photonics. DOI. <https://doi.org/10.1117/12.2528240>.
- Tian, H., DeLuca, E., Reeves, K.K., McKillop, S., De Pontieu, B., Martínez-Sykora, J., Carlsson, M., Hansteen, V., Kleint, L., Cheung, M., Golub, L., Saar, S., Testa, P., Weber, M., Lemen, J., Title, A., Boerner, P., Hurlburt, N., Tarbell, T.D., Wuelser, J.P., Kankelborg, C., Jaeggli, S., McIntosh, S.W.: 2014, High-resolution Observations of the Shock Wave Behavior for Sunspot Oscillations with the Interface Region Imaging Spectrograph. *Astrophys. J.* **786**, 137. DOI. ADS.
- Xia, C., Chen, P.F., Keppens, R., van Marle, A.J.: 2011, Formation of Solar Filaments by Steady and Nonsteady Chromospheric Heating. *Astrophys. J.* **737**, 27. DOI. ADS.